

# Ibn Al-Haitham Journal for Pure and Applied Sciences

Journal homepage: jih.uobaghdad.edu.iq PISSN: 1609-4042, EISSN: 2521-3407 IHJPAS. 2025, 38(4)



# Structural and Microstructural Characterization of Cu-Doped NiFe<sub>2</sub>O<sub>4</sub> Nanoparticles Using Williamson-Hall Method

Sura K. Makki¹<sup>1</sup> ■ and Tagreed M. Al-Saadi²\* ■ ■

<sup>1,2</sup>Department of Physics, College of Education for Pure Sciences (Ibn Al-Haitham), University of Baghdad, Baghdad, Iraq.

\*Corresponding Author.

Received: 8 May 2025 Accepted: 21 August 2025 Published: 20 October 2025

doi.org/10.30526/38.4.4175

#### **Abstract**

In this study report, Cu-doped ferrite nanoparticles (Cu<sub>x</sub>Ni<sub>1-x</sub>Fe<sub>2</sub>O<sub>4</sub>), which are normally the size of less than 100 nanometers were achieved using the sol-gel method. This method consists of using citric acid as fuel, which leads to auto combustion. In this report, the samples mentioned above will be analyzed using the following techniques (XRD, FESEM, EDX), where X-ray diffraction indicated that the specimens consist of spinel phase with facecentered cubic (FCC) structure. The results showed the lattice constant of the material increased from (8.320) Å to (8.323) Å, which indicated fact that the ionic radius of copper (72) Å has a bigger size than the ionic radius of nickel (69) Å which led to an increase in the lattice constant, the crystal size was measured using Scherrer method with the three Williamson Hall models. First, the Williamson Hall Uniform Deformation Model (UDM), second Williamson Hall Uniform Stress Model (USDM), and third Williamson Hall Uniform Deformation Energy Density Model (UDEDM). All these models adapted to define the characteristics related to stress ( $\sigma$ ), internal tendance ( $\epsilon$ ), and deformation energy density (U). The calculated size was compared by the two methods where the crystal size ranged from (19 - 55) nm, and the phenomenon of crystal expansion due to positive stress was observed through the positive slop that appeared in the Williamson Hall models The sample taken was examined further with it morphology character using the method known field emission scanning electron microscopy This has confirmed that the particle shape to be of spherical or sub-spherical, and the size of particle to be within the nano range. The energy-dispersive Xray spectroscopy indicated that no other new elements resulted from this compound.

**Keywords:** Cu<sub>x</sub>Ni<sub>1-x</sub>Fe<sub>2</sub>O<sub>4</sub>, ferrite nanoparticles, X-ray diffraction, Williamson-Hall, Sol-gel

### 1.Introduction

Scientists have focused a lot of interest on nanoparticles; this interest was mainly linked with their size and dimension, for example, nanoparticles size approximately 1-100 nm. Nanoparticles often possess unique size-dependent characteristics, mostly because of their comparatively huge surface area (1-3). This unique identity of the properties of physical and chemical of over bulk materials, interest in nanomaterials, and (particularly nanoparticles) has increased the demand for its usage rapidly in recent decades for different purposes. For example, numerous cutting-edge applications in the domains of electronics, the food industry,

chemical catalysis, medicine and pharmaceuticals, and agriculture have been made available by these exceptional qualities (4). Nanoparticles are generated and synthesized by several procedures, such as the sol-gel method, plasma methodology, vapor phase deposition technique, and electrochemical methods. In spite of these methods of mechanical alloying generating larger amounts of nanoparticles but the sol-gel method has proven to be used on a larger scale in industrial applications. The sol-gel method can generate nanoparticles with extremely high quality and identical size, as well as has more economic advantages; on the other hand, it requires pure raw materials and requires long drying and calcination time to produce the final product (5).

This procedure has several advantages over other synthesis methods, such as being simple to use, inexpensive, producing a larger quantity, and producing large surface area materials. Additionally, it allows for manipulation of the materials' surface characteristics, size, and texture. Because of its ease of usage and versatility, it is frequently utilized in the production of nanoscale powders (6, 7).

Nickel spinel ferrites were not particularly popular with scientists and researchers until Hastings and Corliss published the first reliable study on them. However, because of their new use within different sectors such as sensors of the gas industry, wastewater treatment, radio frequency engineering devices, magnetic separation, biomedical applications, as well as other fields, researchers' interest in nickel spinel ferrites has grown significantly (8, 9). Nickel ferrite (NiFe<sub>2</sub>O<sub>4</sub>) is one of its most prevalent spinel ferrites. Researchers are drawn to its features, which include strong magneto-crystalline anisotropy, unusual magnetic layout, high electrical resistivity, and high Curie temperature (10, 11). NiFe<sub>2</sub>O<sub>4</sub> is a soft ferrimagnetic and n-type semiconducting material (12, 13).

Nickel ferrite belongs to the inverse spinel class represented in the generic context [Fe<sup>3+</sup>] A[Ni<sup>2+</sup>Fe<sup>3+</sup>]BO<sub>4</sub>; furthermore, Fe<sup>3+</sup> can be found on the A-site and B-site, while the B-site is represented by Ni<sup>2+</sup> (14).

In contrast to the size of grains or particles, each isolated particle or grain is composed of many crystal aggregates. The crystallite size can be measured by the Scherrer method, which represents the size of one single crystal within the grains or particles. Crystal imperfections like dislocations and point defects have an impact on lattice strain (15). This can be seen from the Bragg peaks, where the width and intensity have been increased by crystallite size and lattice strain, which leads to a corresponding change within the  $2\theta$  peak position.

The strain changes as  $\tan \theta$  from the width of the peak, while the crystallite size varies as  $1/\cos \theta$ .

The  $2\theta$  difference indicates the influence of size and strain on peak broadening. The W-H analysis is the integral breadth method.

Taking into consideration the peak width, which indicates the function of  $2\theta$ , size-induced and strain-induced broadening are deconvolved (16).

It is well recognized that several factors, such as ion substitution and preparation conditions, affect the characteristics of ferrites. In addition to these factors, the intrinsic strain that these parameters cause on the lattice determines the material's properties. The crystal lattice can experience two different kinds of strain. Crystal lattice under compressive and tensile tension (17).

The X-ray diffraction (XRD) pattern shed light on the lattice strain study, which is considered a crucial structural parameter that may affect the physical properties (18). Doping nickel ferrite with copper ions is an effective way to tune the material's physical and magnetic properties to suit desired applications. Introducing Cu<sup>2+</sup> instead of Ni<sup>2+</sup> changes the unit cell

volume and lattice constant due to different ionic radii, which affects the crystal structure and cation distribution between tetrahydric and octahydric sites. This modification affects magnetic properties such as magnetic saturation and magnetic moments, in addition to improving electrical properties such as conductivity. It can also enhance catalytic properties and thermal stability, making the material more suitable for multiple applications in sensors, catalysts, and solar cells (19)

In this work, the preparation of nickel ferrite nanoparticles by the auto combustion method, the samples was examined by three techniques (XRD, FESEM, EDX); the importance of Scherrer and Williamson-Hall equations in determining the crystal size was revealed through spectra (XRD); important parameters were obtained, namely stress, lattice strain, and energy density, through Williamson-Hall models.

### 2. Materials and Methods

The usage of the Sol-Gel route to prepare nano nickel ferrite doped with copper, like (Cu<sub>x</sub>Ni<sub>1-x</sub>Fe<sub>2</sub>O<sub>4</sub>), where (x=0.05, 0.1). High-purity raw materials ranging between (98 - 99) % were used. These materials include iron nitrate, nickel nitrate, copper nitrate, and citric acid. The citric acid was added to the metal nitrate at a molar ratio of 1:1. The masses of the raw materials were measured using a sensitive balance, as shown in **Table 1**. The dilute raw materials in (40 mL) of deionized which later placed in a glass heat-resistant beaker, and in another beaker, citric acid was mixed with (40 mL) of deionized water. With the magnetic stirrer device, the solutions were mixed without heating until the two solutions became homogeneous. The pH was maintained at 7 by gradually adding drops of ammonia (20). The newly formed solution was heated to 90 °C, resulting in a thick gel. As the heating process continues, the solution begins to dry until auto combustion occurs and a thin black powder resembling ash is obtained. After the solution cools, it is ground in a mortar. The ferrite powder was burned for approximately 120 min at a temperature of (600° C). It was examined using the following techniques (XRD, FE-SEM, EDX) for further observation of the structural properties of the sample.

**Table 1.** The masses of pure raw materials of Cu<sub>x</sub>Ni<sub>1-x</sub>Fe<sub>2</sub>O<sub>4</sub> ferrite.

Sample	$C_6H_8O_7$		Fe (NO <sub>3</sub> ) <sub>3</sub> .9H <sub>2</sub> O		Cu (NO <sub>3</sub> ) <sub>2</sub> .3H <sub>2</sub> O		Ni (NO <sub>3</sub> ) <sub>2</sub> .6H <sub>2</sub> O	
	n	m(g)	n	m(g)	$n_x$	m(g)	$n_{1-x}$	m(g)
F1 (x=0.0)	3	23.0556	2	32.32	0.0	0	1	11.628
F2 (x=0.1)	3	23.0556	2	32.32	0.1	0.9767	0.9	10.465

#### 3.Results

### 3.1. X-Ray Diffraction Patterns

In order to test the phase purity and crystalline properties of the Cu-doped nickel nanoparticles ( $Cu_xNi_{1-x}Fe_2O_4$ ), we will use XRD. The particles prepared by sol-gel method were recorded and shown in Fig. (1), where seven peaks appeared at angles within the range ( $10^\circ$ - $90^\circ$ ) indicating the planes (220), (311), (222), (422), (511), (440), (533), as part of the space group (Fd-3m) No. (227) of the spinel phase with face-centered cubic (FCC) structure. The diffraction peaks of the prepared sample were found to be consistent with the results of JCPDS data No. (19-0629) (21), and no new peaks were observed, indicating the absence of impurities and that the sample had good purity, and the main trends were the planes (222), (422). The lattice constant was determined using the (Match!4) program as shown in **Table 2**, and the ferrite theory density was estimated by X-ray diffraction using the **Equation 1** (22).

$$\rho = \frac{N.M_W}{N_A.V} \tag{1}$$

V denotes unit cell volume, N signifies the number within the unit cell, and Mw represents the molar mass. The results are presented in **Table 2**.

When studying the density changes in  $Cu_xNi_{1-x}Fe_2O_4$  samples, it can be noted that the density decreases slightly when a portion of the nickel ions is replaced by copper ions. Sample F1, which contains no copper (x = 0.0), has a density of 5.34 g/cm<sup>3</sup>, while the density in sample F2 (x = 0.1) decreases to 5.33 g/cm<sup>3</sup>. This decreases, albeit slight, reflects compositional and structural effects within the crystal lattice (**Figure 1**).

Theoretically, the introduction of a heavier element, such as copper, which has a higher atomic mass than nickel, would be expected to result in an increase in density. However, the opposite is observed here. The reason for this discrepancy is the change in the lattice constant, which increases from 8.320 to 8.323 Å upon the introduction of copper. This increase in unit cell volume indicates an expansion of the crystal lattice, leading to a reduction in the number of atoms per unit volume and, consequently, a decrease in density. In addition, the solubility of copper within the lattice and its effect on the redistribution of cations between tetrahedral and octahedral sites may play a role in this change. Copper ions tend to be localized at different sites than nickel ions, contributing to the modification of the microstructure of the composite and affecting the final density of the sample. Therefore, the slight decrease in density reflects a balance between the effect of the atomic mass of the copper ions on the one hand, and the increase in the crystal lattice size and the redistribution of cations on the other (23).

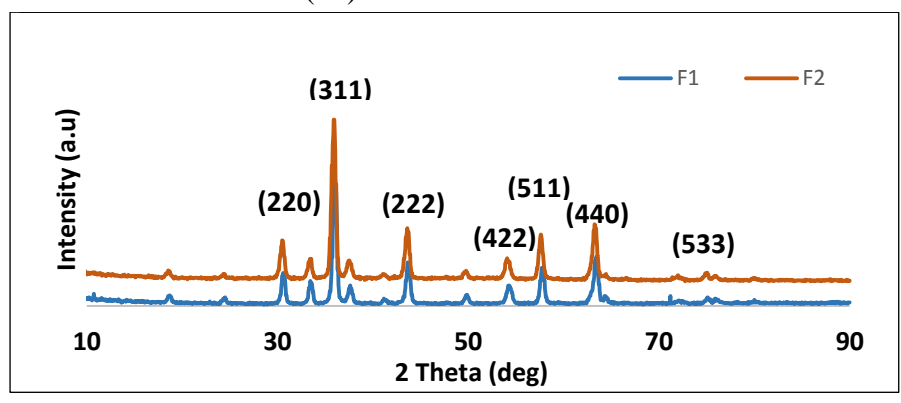


**Figure 1.** X-ray diffraction of Cu<sub>x</sub>Ni<sub>1-x</sub>Fe<sub>2</sub>O<sub>4</sub> samples for x=0.0 (F1) and x=0.1 (F2).

### 3.1.1. The Hopping Length

The spaces between magnetic ions (hopping length) at site A and site B are measured by using the subsequent equations (24).

$$L_A = \frac{a\sqrt{3}}{4} \tag{2}$$

$$L_B = \frac{a\sqrt{2}}{4} \tag{3}$$

The  $(L_A)$  and  $(L_B)$  values calculated above indicate the increase in escalating proportion of copper impurities, and the jump length is associated with the value differences of the lattice constant. This has proved that the value of the jump length  $(L_A)$  is greater than the value of the jump length for  $(L_B)$ , see **Table 2.** 

Table 2. Lattice constant, density, and hopping length to Cu<sub>x</sub>Ni<sub>1-x</sub>Fe<sub>2</sub>O<sub>4</sub>

Sample	a(Å)	Density (g/cm <sup>3</sup> )	$\mathbf{L}_{\mathbf{A}}(\mathbf{\mathring{A}})$	$L_{B}(A)$
F1 (x=0.0)	8.320	5.34	3.59	2.941
F2 (x=0.1)	8.323	5.33	3.60	2.942

### 3.1.2. Texture coefficients (TCs)

The primary purpose of texture coefficients (TCs) is to identify the preferred growth orientation along the (hkl) direction. The samples' advantageous crystallite orientation can be determined in the relationship described below (25, 26).

$$TC_{hkl} = \frac{N*I_{hkl}/I_{ohkl}}{\sum_{N}I_{hkl}/I_{ohkl}}$$
(4)

N represents the reflection number, hkl denotes the Miller indices, Io(hkl) indicates the intensity of (hkl) sourced via JCPDS data No. (19-0629), and I(hkl) indicate the relative intensity recorded for the (hkl) plane. **Table 3** indicates that an increase in copper content affects the texture parameter (TC). A preference for crystal growth was noted at the (222) and (422) lattice planes, whereas a reduction was detected at the (511) and (311) lattice planes, despite some growth occurring at the (311) plane, which, along with the (511) plane, experienced inhibited growth. The decrease in the crystal coordination coefficient of the (511) plane from 0.993 in sample F1 to 0.859 in sample F2 indicates that the introduction of copper ions reduced the preference for crystal growth in this direction. That is due to the difference in ionic properties between Cu<sup>2+</sup> and Ni<sup>2+</sup>, which leads to a redistribution of crystallization directions within the crystal lattice (27).

Table 3. The sample's texture coefficient (Tc) Results

Sample	TC (311)	TC (222)	TC (422)	TC (511)
F1 (x=0.0)	0.975	3.294	1.735	0.993
F2 (x=0.1)	0.975	1.177	1.260	0.859

### 3.2. Determination of Crystallite size & strain

#### 3.2.1. Method of Scherrer

The simplest and efficient technique for assessing peak broadening with crystallite size and strain brought by the dislocation of the peak of XRD profile analysis. The peak broadening is caused by both sample and instrument influences. The instrumental broadening must be completed to determine the magnitude of strain and size effects (28). The instrumental of correction aimed to broaden  $\beta_{hkl}$ , corresponding can be determined by the following (29).

$$\beta^2 = \left[ \left( \beta^2_{\text{measured}} \right) - \left( \beta^2_{\text{instrumental}} \right) \right]^{1/2}$$
 (5)

However, (D) referred to the crystallite size calculated via Scherrer's formula below, as presented below (30, 31)

$$D = \frac{K\lambda}{\beta \cos\theta} \tag{6}$$

In this paper,  $\lambda$  indicates the wavelength of X-ray (1.54056 Å),  $\theta$ , which is the angle of Bragg,  $\beta$  signifies the half maximum of the peak width (in radians), D indicates the crystallite size (nm), while k is the factor (k = 0.94). **Table 4** illustrates the nanoparticles' dimensions.

### 3.2.2. Method of Williamson-Hall

### 3.2.2.1. Uniform deformation model (UDM)

Generally, lattice strain and lattice defects may also have an impact on X-ray diffraction patterns in addition to crystallite size. This analysis can be defined breadth method of Integration, which considers the broadening of the peak width as a function of  $2\theta$  and clearly distinguishes between the deformation peak caused by crystallite size and strain. The expansion of the Bragg reflection line can be calculated (32).

$$\beta_{hkl} = \beta_{s+}\beta_D \tag{7}$$

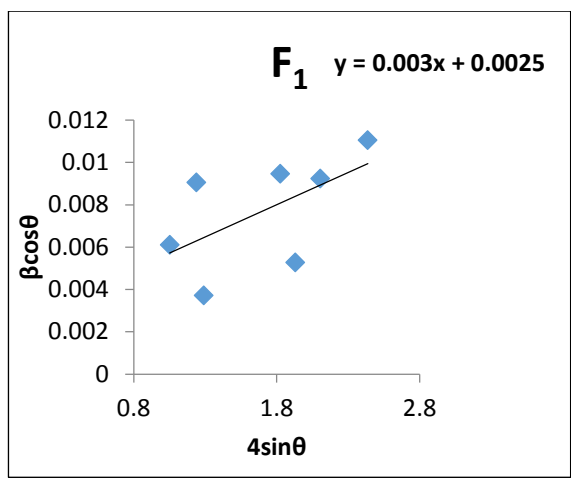
where  $\beta_{s_i}$ ,  $\beta_{D}$  and  $\beta_{hkl}$  Stand for the width caused by size-strain and, correspondingly, the full width at half maximum (FWHM) of a peak. The strain remains uniform along the crystallographic direction in the W–H relationship, which is defined by  $\beta_{hkl}$  and the subsequent relation (33, 34).

$$\beta_o = \frac{\kappa \lambda}{D \cos \theta} + 4\varepsilon \sin \theta \tag{8}$$

Or equivalently,

$$\beta \cos \theta = \frac{\kappa \lambda}{D} + 4\varepsilon \sin \theta \tag{9}$$

Williamson-Hall (W–H) equations are illustrated above, see (8) and (9), which are known as the (UDM). According to the above, crystals should be isotropic since the strain should be constant in all crystallographic orientations. The value of the  $4\sin\theta$  diagram, which represents the x-axis and ( $\beta\cos\theta$ ) values along with the y-axis, together is an indication of the detected diffraction peaks. As can be seen below, the black slop line represents the lattice strain ( $\epsilon$ ), while the y axes (35) <sup>the</sup> crystallite size (D), as shown in **Figure 2**. The nanoparticles' size and strain are shown in **Table 4**.



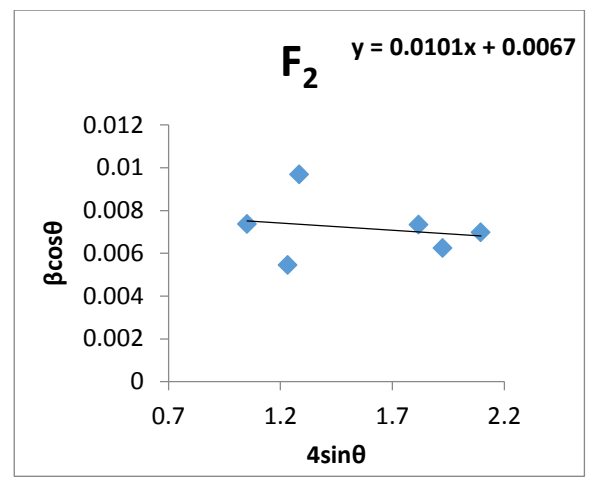


Figure 2. UDM analysis of (Cu<sub>x</sub>Ni<sub>1-x</sub>Fe<sub>2</sub>O<sub>4</sub>) nanoparticles ferrite

#### 3.2.2.2. Uniform stress deformation model (USDM)

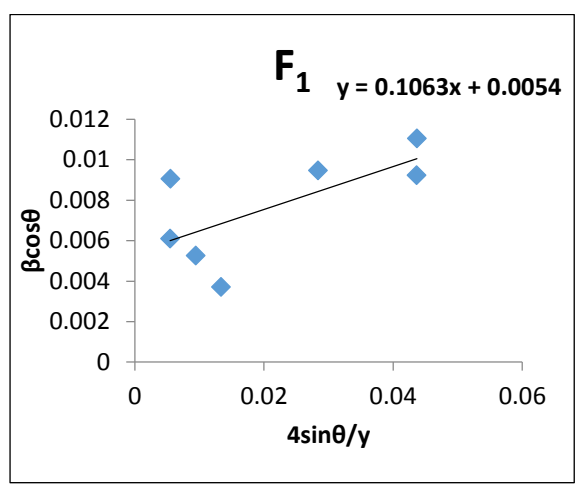
The internal strain explained within Hooke's law in the USDM, this means the linear relations between the stress and strain as provided by  $\sigma = Y\epsilon$ , where the modulus of elasticity and  $\sigma$  is the crystal's stress. This equation only applies to a very modest strain and is only an approximation. Using Hooke's law approximation of the equation, it can obtain the equation below (36).

$$\beta \cos \theta = \frac{K\lambda}{D} + \frac{4\sin \theta}{Y_{hkl}} \tag{10}$$

To calculate the Stress from the slope line drawn between  $(4\sin\theta/Y_{hkl})$  and  $(\beta\cos\theta)$ . Young's modules can be calculated through the following relation.

$$\frac{1}{Y} = S_{11} - (2S_{11} - 2S_{12} - S_{44}) \frac{K^2 L^2 + L^2 h^2 + h^2 k^2}{(h^2 + k^2 + l^2)}$$
(11)

The elastic compatibilities for Fe<sub>3</sub>O<sub>4</sub> are S<sub>11</sub>, S<sub>12</sub>, and S<sub>44</sub>, which are represented by S<sub>11</sub> =  $\frac{(c_{11}+c_{12})}{(c_{11}-c_{12})(c_{11}+2c_{12})}$ ,  $s_{12} = \frac{(-2c_{12})}{(c_{11}-c_{12})(c_{11}+2c_{12})}$  and  $s_{44} = \frac{1}{c_{44}}$ . Where c<sub>11</sub>, c<sub>12</sub>, and c<sub>44</sub> are elastic constant values given by (242.3 GPa), (159.9 GPa), and (55.0 GPa), respectively. USDM plots are displayed in **Figure 3**. The results are shown in **Table 4**.



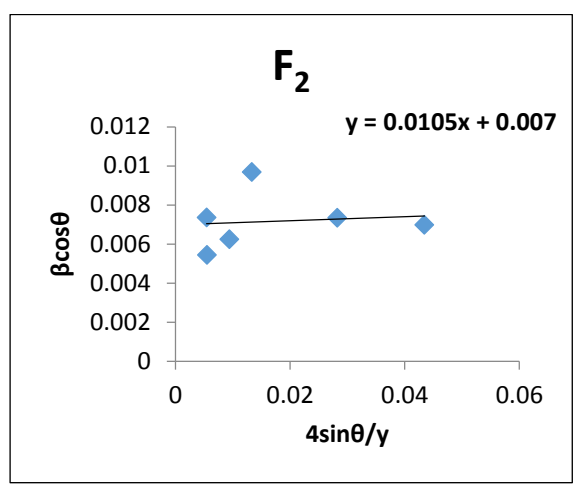


**Figure 3.** The nanoparticles of ferrite through USDM analysis (Cu<sub>x</sub>Ni<sub>1-x</sub>Fe<sub>2</sub>O<sub>4</sub>).

### **3.2.2.3.** Uniform Deformation energy density model (UDEDM)

Another variant of the W-H model employed to analyze lattice energy density of crystals is UDEDM, applicable under conditions of continuous proportionality in homogeneity.

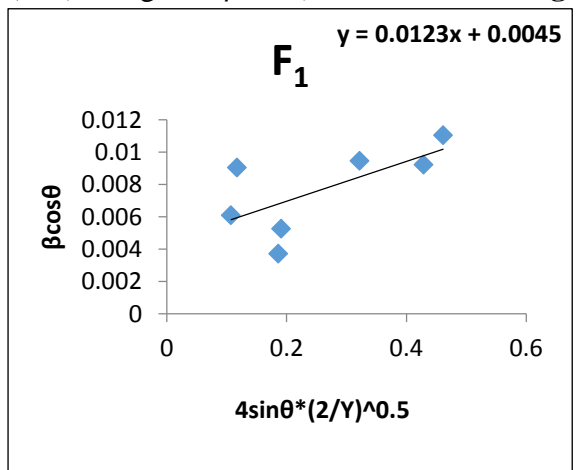
For the calculation of strain, Hooke's law system can be applied (37, 38):

$$U = \frac{\varepsilon^2 Y}{2} \tag{12}$$

From the substitution eq. (12) within eq. (9) resulted in eq. (13)

$$\beta_{hkl}\cos = \frac{\kappa\lambda}{D} + (4\sin\theta \left(\frac{2U}{Y}\right)^{\frac{1}{2}}) \tag{13}$$

The relationship (12) enables lattice stress, strain, and energy density via the graph of  $4\sin\theta$  (2/Y)1/2 against  $\beta\cos\theta$ , as illustrated in **Figure 4**. The findings are presented in **Table 4**.



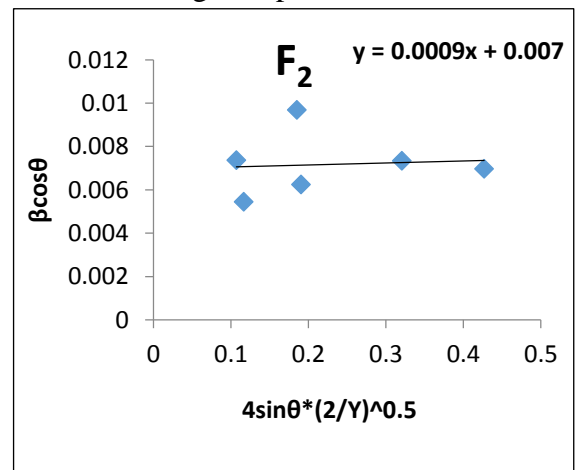


**Figure 4.** The UDEDM analysis of (Cu<sub>x</sub>Ni<sub>1-x</sub>Fe<sub>2</sub>O<sub>4</sub>) nanoparticles ferrite.

Table 4. The result of structure parameters measured by Scherrer and Williamson-Hall methods

	Scherrer method	Williamson-Hall method								
Comple		UDM		USDM			UDEDM			
Sample		D(nm)	ε*10 <sup>-3</sup>	D(nm)	ε*10 <sup>-3</sup>	<b>6*10<sup>-2</sup></b> ( <b>Pa</b> )	D(nm)	ε*10 <sup>-4</sup>	<b>6*10<sup>-2</sup></b> ( <b>Pa</b> )	U*10 <sup>-6</sup> (J.m <sup>-3</sup> )
$F_1$	20.36	55.46	3	25.68	1.2	10.63	30.81	18.4	1.63	151
$F_2$	19.73	20.69	10.1	19.81	0.11	1.05	19.80	0.16	0.161	0.018

#### 3.3. FESEM analysis

Ferrite nanoparticles ( $Cu_xNi_{1-x}Fe_2O_4$ ) are further analyzed via field-emission scanning electron microscopy (FE-SEM) at a scale of 500 nm to determine the nature of the surface and shape of the particles and calculate the average particle size. **Figure 5** shows that the

material falls within the nano range, as its particle size ranges from 56 to 76 nm. The shapes of the particles are organized into crystals formed by distinct grains. These grains are surrounded by grain boundaries that surround each grain. Therefore, the resulting shape is a well-defined grain. It also contains regular, uniform gaps in size and shape, and a few clusters representing unreacted materials. Also, the figure shows the presence of some voids that represent the porous nature, as these pores result from the emission of a quantity of gases during the combustion process (39). In addition to the presence of holes resulting from the inclusion of impurities. Some agglomerations were observed, which are attributed to the fact that the particles have high surface energy and thus tend to agglomerate and grow in larger groups (40).

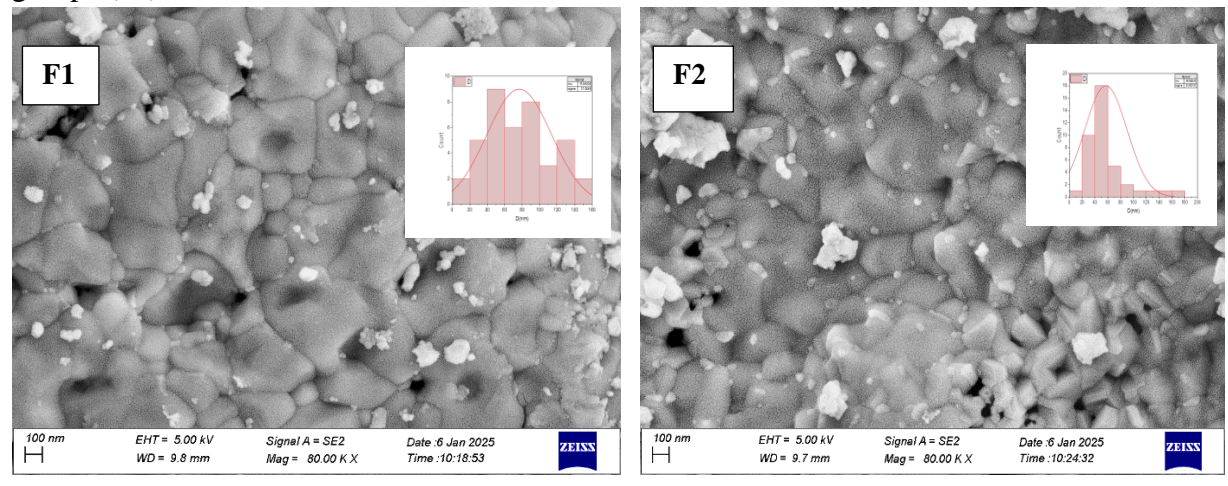


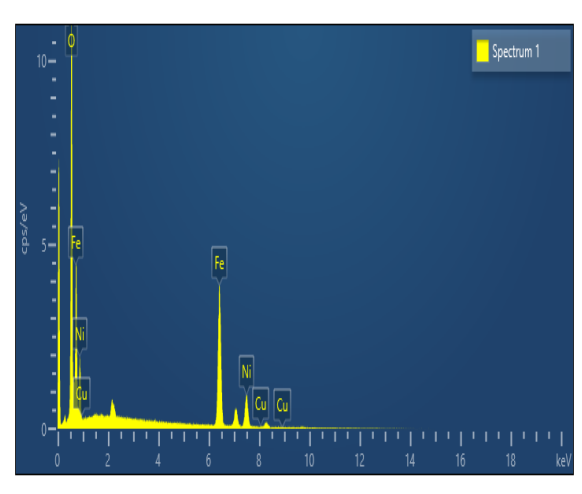
**Figure 5.** FE-SEM image of (Cu<sub>x</sub>Ni<sub>1-x</sub>Fe<sub>2</sub>O<sub>4</sub>) nanoparticles ferrite.

#### 4.Discussion

The obtained chemical composition sample can be used to confirm the atomic composition of the element using spectroscopy (EDX), which later confirmed all elements of the prepared compound solution and confirmed that the samples are pure and free of impurities. The data confirmed the success of the auto combustion process due to the absence of elemental loss during the auto combustion process. The presence of copper (Cu) in the F1 sample assay is likely due to copper contamination of the sample during preparation, processing, previous use of the equipment, a software error, or other reasons. The peaks of the elements (Fe, O, Ni, Cu) appeared clearly, where the peaks of the nickel element appeared at energies (K $\alpha$  = 7.480 KeV),(L $\alpha$  =0.849 KeV), the peaks of the oxygen element appeared at energy (L $\alpha$  =0.525 keV), the peaks of the iron element appeared at energies (K $\alpha$  =6.931KeV), (L $\alpha$  =0.775KeV), and the peaks of the copper element appeared at energies (L $\alpha$  =8.046 keV), (K $\alpha$  = 0.928 keV), as shown in **Figure 6** and **Table 5** shows the weight and atomic composition percentage of the elements.

**Table 5.** The weight and atomic composition percentage of the elements.

Sample	Element	Line Type	Atomic%	Wt%
	0	Κα	67.87	37.37
T.	Fe	Κα & Lα	23.09	44.38
$\mathbf{F}_1$	Ni	Κα & Lα	0.04	18.25
	Cu	Κα & Lα	0.00	0.00
	O	Κα	62.65	32.21
17	Fe	Κα & Lα	30.31	54.40
$F_2$	Ni	Κα & Lα	0.66	1.36
	Cu	Κα & Lα	6.38	12.03



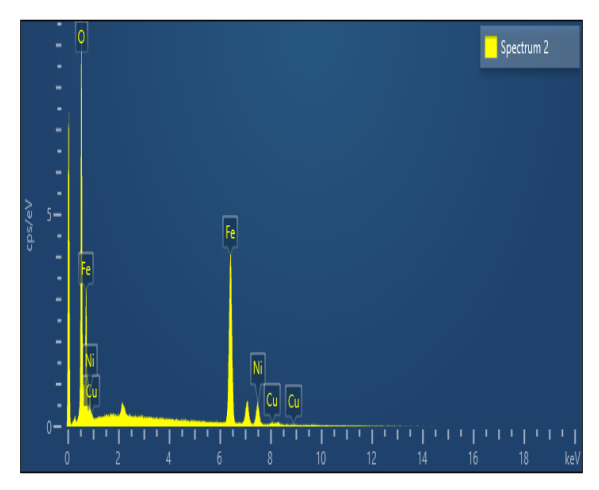


Figure 6. EDX analysis of (Cu<sub>x</sub>Ni<sub>1-x</sub>Fe<sub>2</sub>O<sub>4</sub>) nanoparticles ferrite.

#### 5. Conclusions

Cu<sub>x</sub>Ni<sub>1-x</sub>Fe<sub>2</sub>O<sub>4</sub> nanoparticles were prepared using a simple and low-cost auto combustion process. Analyses (FE-SEM, XRD, EDX) revealed that all samples consisted of spinel ferrite nanoparticles with a single-phase cubic (FCC) structure, exhibiting no new peaks. The shapes of the particles are organized into crystals formed by distinct grains. This work revealed that the classical X-ray diffraction (XRD) analysis method (Scherrer method) gives inaccurate estimates of crystal size and does not give strain values. Therefore, the Williamson-Hall method has three models. The three Williamson-Hall models are compared here, and they are found to provide different aspects of stress and strain of nanocrystals. The UDM (Uniform Deformation Model) assumes that strain is uniform in all crystallographic directions, making it the simplest model, but overlooking elastic properties. USDM (Uniform Stress Deformation Model) is based on Hooke's law, in which stress and strain are linearly related by Young's modulus. This provides a more accurate value for internal stress. The UDEDM (Uniform Deformation Energy Density Model) considers deformation energy density and so provides the most comprehensive model for analyzing energy stored in a crystal lattice because of deformation. Experiments on the studied sample Cu<sub>x</sub>Ni<sub>1-x</sub>Fe<sub>2</sub>O<sub>4</sub> showed stress and strain values to differ between models. Here, UDM measured the highest strain value  $(10.1\times10^{-3})$  in comparison with USDM  $(0.11\times10^{-3})$  and UDEDM  $(0.16\times10^{-4})$ , confirming that one should select the model according to the nature of the sample and analysis target.

#### Acknowledgment

I would like to thank the staff of the Physics Department, Deanship of the College of Education for Pure Science (Ibn Al-Haitham), for their support in writing this research.

### **Conflict of Interest**

The authors declare that they have no conflicts of interest.

#### **Funding**

None.

#### References

- 1. Najahi-Missaoui W, Arnold RD, Cummings BS. Safe nanoparticles: are we there yet? Int J Mol Sci. 2020;22(1):385. <a href="https://doi.org/10.3390/ijms22010385">https://doi.org/10.3390/ijms22010385</a>.
- 2. Mohajerani A, Burnett L, Smith JV, Kurmus H, Milas J, Arulrajah A, Horpibulsuk S, Abdul Kadir A. Nanoparticles in construction materials and other applications, and implications of nanoparticle use. Mater. 2019;12(19):3052. https://doi.org/10.3390/ma12193052.

- 3. Liu P, Ma S, Zhang J, Huang Y, Liu Y, Wang Z. Formation of ultra-stable Au nanoparticles in Au–ZrO2 nanocomposites. J Mater Sci Technol. 2025;217:104-115. https://doi.org/10.1016/j.jmst.2024.08.007.
- 4. Joudeh N, Linke D. Nanoparticle classification, physicochemical properties, characterization, and applications: a comprehensive review for biologists. J Nanobiotechnol. 2022;20(1):262. https://doi.org/10.1186/s12951-022-01477-8.
- 5. Bokov D, Turki Jalil A, Chupradit S, Suksatan W, Javed Ansari M, Shewael IH, Valiev GH, Kianfar E. Nanomaterial by sol-gel method: synthesis and application. Adv Mater Sci Eng. 2021;2021(1):5102014. https://doi.org/10.1155/2021/5102014.
- 6. Maikudi S, Alhadhrami A, Alshdoukhi IF, Ibrahim MM, Abouzied AS, Zaki ZI, Fallatah AM, Mohammed J. Cs3+-Ni2+ substituted spinel ferrites nanoparticles: insights into the crystal structure and magneto-optical properties. J Mol Struct. 2025;1332:141665. https://doi.org/10.1016/j.molstruc.2025.141665.
- 7. Navas D, Fuentes S, Castro-Alvarez A, Chavez-Angel E. Review on sol-gel synthesis of perovskite and oxide nanomaterials. Gels. 2021;7(4):275. https://doi.org/10.3390/gels7040275.
- 8. Narang SB, Pubby K. Nickel spinel ferrites: a review. J Magn Magn Mater. 2021;519:167163. https://doi.org/10.1016/j.jmmm.2020.167163.
- 9. Reddy BC, Manjunatha HC, Vidya YS, Sridhar KN, Pasha UM, Seenappa L, Mahendrakumar C, Sadashivamurthy B, Dhananjaya N, Sankarshan BM, Krishnaveni S. Synthesis and characterization of multifunctional nickel ferrite nanoparticles for X-ray/gamma radiation shielding, display and antimicrobial applications. J Phys Chem Solids. 2021;159:110260. https://doi.org/10.1016/j.jpcs.2021.110260.
- 10.Jadhav SA, Khedkar MV, Somvanshi SB, Jadhav KM. Magnetically retrievable nanoscale nickel ferrites: an active photocatalyst for toxic dye removal applications. Ceram Int. 2021;47(20):28623-28633. https://doi.org/10.1016/j.ceramint.2021.07.021.
- 11. Aggarwal D, Kaur M, Bansal S, Singhal S. Fabrication of eco-friendly NiFe2O4 nanocatalysts via plant extract-mediated synthesis: kinetic and mechanistic insights into photocatalytic degradation of an anthraquinone dye and tetracycline antibiotic. J Mol Struct. 2025;1319:139365. https://doi.org/10.1016/j.molstruc.2024.139365.
- 12. Paswan SK, Kumari S, Kar M, Singh A, Pathak H, Borah JP, Kumar L. Optimization of structure-property relationships in nickel ferrite nanoparticles annealed at different temperature. J Phys Chem Solids. 2021;151:109928. https://doi.org/10.1016/j.jpcs.2020.109928.
- 13. Arrasheed EA, Meaz TM, Shalaby RM, Salem BI, Hemeda OM, Henaish AM. Rietveld refinement, cation distribution, morphological and magnetic study of NiAlxFe2-xO4 nanoparticles. Appl Phys A. 2021;127:1-10. https://doi.org/10.1007/s00339-021-04360-9.
- 14.Dey B, Bououdina M, Dhamodharan P, AsathBahadur S, Venkateshwarlu M, Manoharan C. Tuning the gas sensing properties of spinel ferrite NiFe2O4 nanoparticles by Cu doping. J Alloys Compd. 2024;970:172711. https://doi.org/10.1016/j.jallcom.2023.172711.
- 15.Irfan H, Racik KM, Anand S. X-ray peak profile analysis of CoAl2O4 nanoparticles by Williamson-Hall and size-strain plot methods. Mod Electron Mater. 2018;4(1):31-40. <a href="https://doi.org/10.3897/j.moem.4.1.33272">https://doi.org/10.3897/j.moem.4.1.33272</a>.
- 16.Desai KR, Alone ST, Wadgane SR, Shirsath SE, Batoo KM, Imran A, Raslan EH, Hadi M, Ijaz MF, Kadam RH. X-ray diffraction based Williamson–Hall analysis and Rietveld refinement for strain mechanism in Mg–Mn co-substituted CdFe2O4 nanoparticles. Phys B Condens Matter. 2021;614:413054. https://doi.org/10.1016/j.physb.2021.413054.
- 17.Desai KR, Alone ST, Wadgane SR, Shirsath SE, Batoo KM, Imran A, Raslan EH, Hadi M, Ijaz MF, Kadam RH. X-ray diffraction based Williamson–Hall analysis and Rietveld refinement for strain mechanism in Mg–Mn co-substituted CdFe2O4 nanoparticles. Phys B Condens Matter. 2021;614:413054. <a href="https://doi.org/10.1016/j.physb.2021.413054">https://doi.org/10.1016/j.physb.2021.413054</a>.
- 18.Maniammal K, Madhu G, Biju V. X-ray diffraction line profile analysis of nanostructured nickel oxide: shape factor and convolution of crystallite size and microstrain contributions. Phys E Low Dimens Syst Nanostruct. 2017;85:214-222. <a href="http://dx.doi.org/10.1016/j.physe.2016.08.035">http://dx.doi.org/10.1016/j.physe.2016.08.035</a>.

- 19. Anjana V, John S, Prakash P, Nair AM, Nair AR, Sambhudevan S, Shankar B. Magnetic properties of copper doped nickel ferrite nanoparticles synthesized by co-precipitation method. IOP Conf Ser Mater Sci Eng. 2018;310(1):012024. <a href="https://doi.org/10.1088/1757-899X/310/1/012024">https://doi.org/10.1088/1757-899X/310/1/012024</a>.
- 20.Al-Saadi TM, Abed AH, Salih AA. Synthesis and characterization of AlyCu0.15Zn0.85-yFe2O4 ferrite prepared by the sol-gel method. Int J Electrochem Sci. 2018;13(9):8295-8302. https://doi.org/10.20964/2018.09.04.
- 21.Namikuchi EA, Gaspar RD, da Silva DS, Raimundo IM, Mazali IO. PEG size effect and its interaction with Fe3O4 nanoparticles synthesized by solvothermal method: morphology and effect of pH on the stability. Nano Express. 2021 Jun 4;2(2):020022. DOI: 10.1088/2632-959X/ac0596
- 22.Mustafa HJ, Al-Saadi TM. Effects of gum arabic-coated magnetite nanoparticles on the removal of Pb ions from aqueous solutions. Iraqi J Sci. 2021;62(3):889-896. https://doi.org/10.24996/ijs.2021.62.3.20.
- 23. Pender JP, Jha G, Youn DH, Ziegler JM, Andoni I, Choi EJ, Heller A, Dunn BS, Weiss PS, Penner RM, Mullins CB. Electrode degradation in lithium-ion batteries. ACS Nano. 2020;14(2):1243-1295. https://doi.org/10.1021/acsnano.9b04365.
- 24.Shashidhargouda HR, Mathad SN. Synthesis and structural analysis of Ni0.45Cu0.55Mn2O4 by Williamson–Hall and size–strain plot methods. Ovidius Univ Ann Chem. 2018;29(2):122-125. https://doi.org/10.2478/auoc-2018-0018.
- 25.Norouzzadeh P, Mabhouti K, Golzan MM, Naderali R. Consequence of Mn and Ni doping on structural, optical and magnetic characteristics of ZnO nanopowders: the Williamson–Hall method, the Kramers–Kronig approach and magnetic interactions. Applied Physics A. 2020 Mar;126(3):154. DOI: 10.1007/s00339-020-3335-9
- 26.Atre PP, Desai MA, Vyas AN, Sartale SD, Pawar BN. Deposition of  $\beta$ -In2S3 photosensitive thin films by ultrasonic spray pyrolysis. ES Energy Environ. 2020;12:52-59. https://doi.org/10.30919/esee8c1041.
- 27. Siegfried MJ, Choi KS. Elucidating the effect of additives on the growth and stability of Cu2O surfaces via shape transformation of pre-grown crystals. J Am Chem Soc. 2006;128(32):10356-10357. https://doi.org/10.1021/ja063574y.
- 28.Aly KA, Khalil NM, Algamal Y, Saleem QM. Lattice strain estimation for CoAl2O4 nanoparticles using Williamson–Hall analysis. J Alloys Compd. 2016;676:606-612. https://doi.org/10.1016/j.jallcom.2016.03.213.
- 29. Sivakami R, Dhanuskodi S, Karvembu R. Estimation of lattice strain in nanocrystalline RuO2 by Williamson–Hall and size–strain plot methods. Spectrochim Acta A Mol Biomol Spectrosc. 2016;152:43-50. <a href="http://dx.doi.org/10.1016/j.saa.2015.07.008">http://dx.doi.org/10.1016/j.saa.2015.07.008</a>.
- 30.Mahdi HI, Bakr NA, Al-Saadi TM. Studying the gas sensitivity and magnetic properties of magnesium ferrite prepared by the sol-gel route. Iraqi J Sci. 2024;65(8):4313-4324. https://doi.org/10.24996/ijs.2024.65.8.16.
- 31.Kawsar M, Hossain MS, Bahadur NM, Ahmed S. Synthesis of nano-crystallite hydroxyapatites in different media and a comparative study for estimation of crystallite size using Scherrer method, Halder-Wagner method size-strain plot, and Williamson-Hall model. Heliyon. 2024 Feb 15;10(3). <a href="https://doi.org/10.1016/j.heliyon.2024.e25347">https://doi.org/10.1016/j.heliyon.2024.e25347</a>
- 32.Monshi A, Foroughi MR, Monshi MR. Modified Scherrer equation to estimate more accurately nano-crystallite size using XRD. World journal of nano science and engineering. 2012 Sep 28;2(3):154-60. DOI: 10.4236/wjnse.2012.23020
- 33.Mahdi HI, Al-Saadi TM, Bakr NA. Fabrication and characterization of CoxMn0.25-xMg0.75Fe2O4 nanoparticles for H2S sensing applications. J Mater Sci Mater Electron. 2023;34(22):1634. https://doi.org/10.1007/s10854-023-11064-8.
- 34.Al-Saadi TM, Kamil ZA. Study the effect of manganese ion doping on the size-strain of SnO2 nanoparticles using X-ray diffraction data. Ibn Al-Haitham J Pure Appl Sci. 2023;36(3):158-166. <a href="https://doi.org/10.30526/36.3.3052">https://doi.org/10.30526/36.3.3052</a>.

- 35. Sundaram PS, Sangeetha T, Rajakarthihan S, Vijayalaksmi R, Elangovan A, Arivazhagan G. XRD structural studies on cobalt doped zinc oxide nanoparticles synthesized by coprecipitation method: Williamson-Hall and size-strain plot approaches. Phys B Condens Matter. 2020;595:412342. <a href="https://doi.org/10.1016/j.physb.2020.412342">https://doi.org/10.1016/j.physb.2020.412342</a>.
- 36.Nath D, Singh F, Das R. X-ray diffraction analysis by Williamson-Hall, Halder-Wagner and size-strain plot methods of CdSe nanoparticles-a comparative study. Mater Chem Phys. 2020;239:122021. https://doi.org/10.1016/j.matchemphys.2019.122021.
- 37.Himabindu B, Devi NL, Kanth BR. Microstructural parameters from X-ray peak profile analysis by Williamson-Hall models; a review. Mater Today Proc. 2021;47:4891-4896. <a href="https://doi.org/10.1016/j.matpr.2021.06.256">https://doi.org/10.1016/j.matpr.2021.06.256</a>.
- 38.Dey PC, Das R. Impact of silver doping on the crystalline size and intrinsic strain of MPA-capped CdTe nanocrystals: a study by Williamson–Hall method and size–strain plot method. J Mater Eng Perform. 2021;30:652-660. <a href="https://doi.org/10.1007/s11665-020-05358-9">https://doi.org/10.1007/s11665-020-05358-9</a>.
- 39.Haija MA, Abu-Hani AF, Hamdan N, Stephen S, Ayesh AI. Characterization of H2S gas sensor based on CuFe2O4 nanoparticles. J Alloys Compd. 2017;690:461-468. https://doi.org/10.1016/j.jallcom.2016.08.174.
- 40.Sagadevan S, Chowdhury ZZ, Rafique RF. Preparation and characterization of nickel ferrite nanoparticles via co-precipitation method. Mater Res. 2018;21:e20160533. https://doi.org/10.1590/1980-5373-MR-2016-0533.